ROYAL SOCIETY OF CHEMISTRY

Check for updates

Near-cryogenic direct air capture using adsorbents†‡

Seo-Yul Kim, [ID] [a] Akriti Sarswat, [ID] [a] Sunghyun Cho, [b] MinGyu Song, [a] Jinsu Kim, [ID] [c] Matthew J. Realff, [ID] [a] David S. Sholl [d] and Ryan P. Lively [ID] *[a]

Direct air capture (DAC) of CO_2 is a key component in the portfolio of negative emissions technologies for mitigating global warming. However, even with the most potent amine sorbents, large-scale DAC deployment remains limited by high energy and capital costs. Recently, adsorbents relying on weak interactions with CO_2 have emerged as a potential alternative, thanks to their rapid adsorption kinetics and superior long-term stability, particularly under sub-ambient conditions ($\sim$253 K). Despite these advantages, their use is hindered by the need for a water-removal process, location-specific constraints, and insufficient working capacity even in cold climates. In this study, we hypothesized that further reducing the adsorption temperature to a near-cryogenic range (160–220 K) could enable cost-effective DAC by utilizing the full potential of physisorbents. We primarily consider integrating DAC with a relatively untapped source of cold energy—liquified natural gas (LNG) regasification—to perform near-cryogenic DAC. From large-scale molecular simulations, Zeolite 13X and CALF-20 were identified as promising candidates. These materials were subsequently examined through experiments, including breakthrough analyses at 195 K. Their high CO_2 sorption capacity (4.5–5.5 mmol g^{-1}), combined with a low desorption enthalpy and robust long-term stability, led to a threefold reduction in the levelized cost of capture (down to 68.2 USD per tonne CO_2). Estimates of the global LNG regasification resource suggest that LNG–DAC coupling could potentially enable the capture of 103–142 megatonnes of CO_2 annually as of 2050.

Broader context

Global-scale adoption of negative emissions technologies like direct air capture (DAC) is essential for all climate targets that maintain global surface temperatures below +3.0 °C relative to pre-industrial levels. However, DAC remains too costly for such widespread deployment and too energy-intensive for near-term viability, given the pace of energy sector decarbonization. The primary energy demand for DAC comes from the heat required to regenerate CO_2 capture sorbents. Heat demand is typically determined by the sorbent and the capture process. Two pathways towards low-cost DAC are the use of robust sorbents with low energy requirements and the integration of largely untapped energy sources. In this work, we propose a process that achieves both: DAC at near-cryogenic temperatures obtained *via* integration with liquefied natural gas (LNG) regasification. Multi-scale assessment, including molecular simulations, experiments, and techno-economic analysis, demonstrates that near-cryogenic conditions enable cost- and energy-efficient DAC using durable, low-cost sorbents (Zeolite 13X and CALF-20) with minimal regeneration energy. Our analysis estimates the net energy demand at 1.7–3.3 gigajoules per tonne of CO_2—far lower than conventional DAC, which requires more than 7 GJ per tonne—along with approximately 60% reduction in cost. This approach presents a promising pathway to making DAC a viable near-term solution.

[a] *School of Chemical and Biomolecular Engineering, Georgia Institute of Technology, Atlanta, GA 30332, USA. E-mail: ryan.lively@chbe.gatech.edu*

[b] *School of Chemical Engineering, School of Semiconductor and Chemical Engineering, Clean Energy Research Center, Jeonbuk National University, JeonJu, Jeonbuk 54896, Republic of Korea*

[c] *Department of Petrochemical Materials, Chonnam National University, 50 Daehak-ro, Yeosu-si, 59631, Republic of Korea*

[d] *Oak Ridge National Laboratory, Oak Ridge, TN 37830, USA*

This journal is © The Royal Society of Chemistry 2025

Energy Environ. Sci., 2025, **18**, 7427–7439 | 7427

Introduction

Direct air capture of CO_2 (DAC)[1–5] is a key component of many of the climate scenarios in which global surface temperatures are stabilized within +1.5–2.0 °C relative to pre-industrial times.[6,7] Despite promising candidate processes and materials for DAC developed over the last decade, the high capital and energy costs of DAC have limited its deployment to date.[8–10]

The energy required to recover captured CO_2 during DAC as a purified product is a significant issue. Solid adsorbents, such as amine-impregnated porous oxides, have among the lowest overall energy requirements for DAC processes, with lower-bound estimates for total energy penalty ranging from 4–6 GJ per tonne of CO_2 (tCO$_2$), although energies in excess of 7 GJ per tCO$_2$ are commonly realized in practice.[5,11–13] Moreover, DAC also requires large capital costs,[13,14] which largely depend on the performance of sorbent materials, including the working capacity, adsorption kinetics, long-term stability, and price.[5,15,16] Unfortunately, the most promising DAC sorbents to date, supported amine sorbents, have limitations in working capacity (~ 2.5 mmol g_{powder}^{-1}), adsorption kinetics, and oxidative stability. Moreover, most DAC sorbent materials also adsorb significant quantities of water from ambient air, and water removal or desorption is often a major energy penalty.[17,18]

Recently metal–organic frameworks (MOFs) selected for physisorption-based DAC processes have garnered interest due to favorable adsorption kinetics and low CO_2 desorption enthalpies.[19] A handful of physisorbing MOFs out of the $\sim 60\,000$ experimentally synthesized MOF materials have been suggested as having sufficient CO_2 selectivity for DAC.[20,21] However, these materials significantly underperformed amine-based materials in realistic DAC experiments, largely due to issues associated with water co-adsorption.[13,20,22] In addition, MOFs often require expensive precursors and, to date, only a very small selection of MOFs have been scaled up. Recent work showed that commercially-available zeolites could exhibit moderate DAC performance at sub-ambient temperatures (−20 °C to 0 °C); however, they require a separate water removal process and do not have CO_2 working capacity advantages over amine sorbents operating at ambient conditions and without water removal.[23] The DAC sorption capacity of zeolites was further evaluated at a much lower temperature of −58 °C, where atmospheric air can be assumed to be nearly dry. However, even under these extremely low-temperature conditions, which are naturally achievable but limited to very specific regions and seasons, the sorption capacity of zeolites did not surpass that of conventional amine sorbents.[24]

DAC at lower temperatures, unattainable for atmospheric air under natural conditions, can fully utilize the capacity of adsorbents with low heats of adsorption for CO_2. Atmospheric air cooling to 120–150 K to directly sublime atmospheric CO_2 ('cryogenic DAC') was found to be infeasible due to the substantial energy required for cooling.[25,26] However, compared to direct sublimation, physisorption can facilitate DAC at higher near-cryogenic temperatures (160–240 K), significantly reducing air cooling enthalpy and the capital associated with specialized cryogenic equipment. Nevertheless, it remains essential to leverage "free" sources of cold energy (e.g., energy recovery) to consider deploying near-cryogenic DAC in warmer regions and extend its broader impact.[27]

Liquefied Natural Gas (LNG) regasification systems are currently an untapped source of cold energy.[28] In these systems, LNG is vaporized at terminals into natural gas (NG). These terminals operate at large scale in coastal regions, and the latent heat of vaporization is transferred to seawater and exhausted back into the ocean.[29] Indeed, about 95% of the regasification processes are conducted by heat exchange with seawater, which wastes the exergy (i.e., the available energy capable of doing useful work) of LNG and also raises concerns for local ecosystems.[29,30] The regasification process can be integrated by heat exchange with other processes instead, including the Rankine vapor cycle,[31,32] air separation unit (ASU),[33] adsorbed natural gas,[34,35] and post-combustion CO_2 capture,[36,37] to provide cold energy to those processes.

In this study, we hypothesize that the cold energy from LNG regasification or other available external cooling cycles can enable cost-efficient DAC at near-cryogenic temperatures (160–240 K). DAC at near-cryogenic temperatures is expected to enable the use of adsorbents with low heats of adsorption for CO_2, which can reduce energy and capital costs via significant enhancements in working capacity.[38–42] Part of the cold energy provided by LNG regasification or a cooling loop can be used to condense out the water vapor in air during the early stages of heat exchange, resulting in cold air with sub-ppm levels of water vapor. This low water concentration also enables the use of many physisorbents that have previously been ruled out for DAC.

The potential of physisorbents under near-cryogenic DAC conditions was initially evaluated through large-scale grand canonical Monte Carlo (GCMC) simulations of the CoRE-MOF database with density derived electrostatic and chemical (DDEC) charges.[43] Notably, the structure–property relationships learned from the CoRE-MOF database are not confined to MOFs and can be extended to other classes of sorbents.[44] Based on these simulations, CO_2 adsorption equilibrium uptakes of four physisorbents–MIL-120(Al),[45] Zeolite 5A, Zeolite 13X,[23,46] and CALF-20[47]–were examined under various near-cryogenic temperatures in volumetric adsorption apparatuses. Among these adsorbent candidates, Zeolite 13X and CALF-20 were selected and further examined by dynamic breakthrough analysis at 195 K. The experimental results were used to perform techno-economic analyses of near-cryogenic DAC processes incorporating thermal coupling with LNG regasification. The potential scale of carbon capture via LNG–DAC deployment was also assessed to illustrate the long-term impact of the concept on global climate change scenarios.

Results and discussion

Identifying promising adsorbents via large-scale GCMC simulation

In LNG regasification, the vaporization temperature of LNG can vary between 109 and 190 K depending on the storage pressure

7428 | Energy Environ. Sci., 2025, **18**, 7427–7439

This journal is © The Royal Society of Chemistry 2025

of LNG.[48] After vaporization, the natural gas is heated to around room temperature (up to 283 K) before being supplied into pipeline networks. Therefore, the thermal coupling of DAC with LNG regasification can enable adsorption temperatures between 109 K and 283 K. In this study, a suitable range of adsorption temperature for the near-cryogenic DAC process was assumed to be between 160 and 220 K (Fig. 1A). At temperatures lower than 160 K, it is likely that competitive adsorption of O_2 and N_2 will become an issue for CO_2 product purity and recovery. At temperatures higher than 220 K, there are simply too few physisorbents that can successfully capture CO_2 from air with a high working capacity. An important feature of this approach is that cooling air to 160–220 K removes nearly all water that is present in ambient air *via* condensation.[49,50] For example, 50% relative humidity at 283 K corresponds to 6100 ppm water vapor, but the same relative humidity at 160 K yields a water concentration of only 3.95×10^{-4} ppm (Fig. S1, ESI‡).

In the proposed DAC process coupled with LNG regasification, the feed air flow is first cooled to the adsorption temperature of the adsorbent materials (160–220 K). The cooling is achieved by heat exchange in the LNG evaporator, and during the process the water vapor in the air almost completely freezes out.[51] Alternatively, the water vapor could condense and be removed before freezing during the initial few heat exchanger stages, as previously proposed for an air separation unit (ASU) coupled to the LNG evaporator (Fig. S1, ESI‡).[50,52] If necessary, trace amounts of residual moisture after cooling can be removed with a small amount of desiccant to ensure complete

dehydration. Regardless, the cold, dry air passes through the adsorbent bed, simultaneously cooling the bed and introducing CO_2 for capture (Fig. 1A). In this process, the cold energy from the LNG regasification process is used to compensate for four enthalpy changes: (1) cooling the feed air, (2) cooling and condensing or freezing water, (3) cooling the adsorbent bed, and (4) mitigating heating of the adsorption bed due to CO_2 adsorption.[34,35] After the adsorption process, the bed is isolated from gas flow and heated up to around room temperature ($\sim$283 K) by heat exchanging with seawater. If this temperature is insufficient for recovery of the given sorbent, it can be further increased to a higher desorption temperature (*e.g.*, 473 K) by external thermal energy (*e.g.*, heat from natural gas combustion). Various desorption processes can be considered depending on the characteristics of the sorbent used. Notably, the near-cryogenic DAC has the potential to utilize physisorbents, which are suitable for desorption with high-purity CO_2 as a desorbent gas at elevated temperature ($>$423 K), at which amine sorbents may become unstable. Using high-purity CO_2 to sweep desorbed CO_2 out of the bed can achieve high CO_2 product purity and obviate the need for vacuum systems (Fig. 1B).[23] Alternatively, vacuum-assisted desorption at relatively lower temperatures could also be considered to reduce thermal energy costs (Fig. 1C). It is worth noting that the cycle can also produce fresh water[53] and pre-cooled air for an ASU, which could generate additional profit. However, the potential cost reduction from these byproducts was not included in this study due to uncertainty about whether their future demand will align with the substantial production volumes from the DAC process.
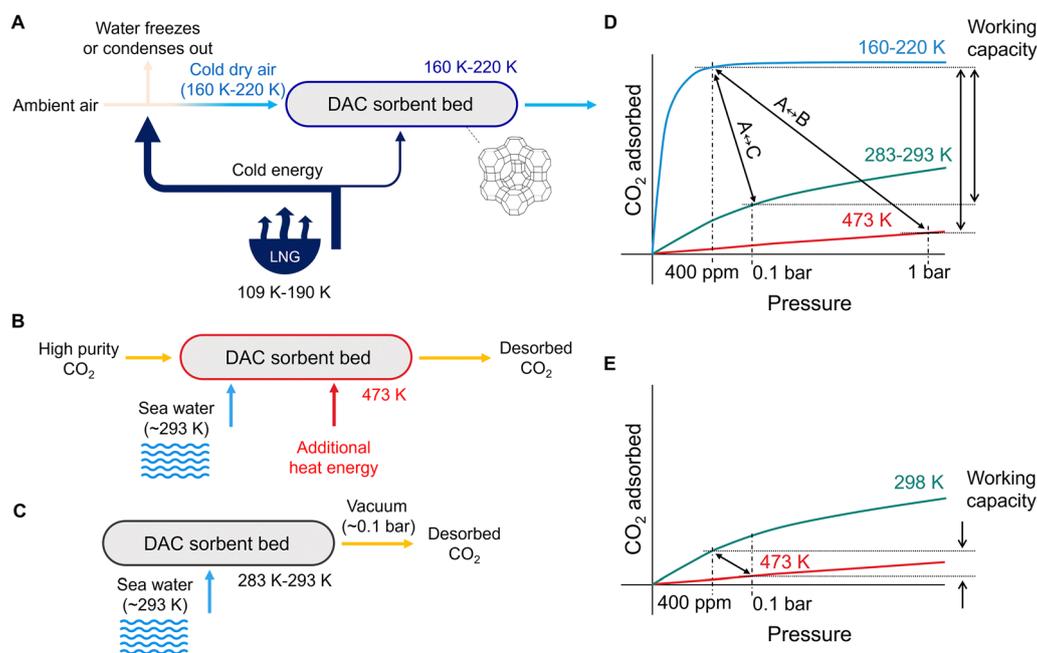
Fig. 1 Schematic illustration of the LNG–DAC coupling and near-cryogenic DAC processes. (A) Adsorption of CO_2 from the cold, dry air (160–220 K) produced by heat exchange with LNG regasification. (B) Desorption of CO_2 and recovery at 473 K using a CO_2 sweep gas. (C) Desorption of CO_2 at 283–293 K without external thermal energy but aided by a vacuum pump. Representative CO_2 isotherms and adsorption–desorption conditions for typical physisorbents during temperature (vacuum) swing adsorption between (D) near-cryogenic DAC conditions and the suggested desorption conditions, (E) room temperature and elevated temperature.

This journal is © The Royal Society of Chemistry 2025

Energy Environ. Sci., 2025, **18**, 7427–7439 | **7429**

As mentioned earlier, DAC at near-cryogenic temperatures is expected to enable the use of physisorbents with low heats of adsorption.[23,24,54,55] These physisorbents have insufficient interaction with CO_2 for room-temperature DAC and typically have very low CO_2 uptake from the ambient air (Fig. 1E). However, exothermic physisorption is thermodynamically much more favored at near-cryogenic temperatures and can result in high working capacity (Fig. 1D).

Exact prediction of the CO_2 adsorption behavior of individual MOFs at highly dilute conditions (0.0004 bar) by molecular simulations with a generic force field is very challenging because of potential influences from framework flexibility and defects in addition to the precision of the force fields;[56,57] however, their trends are still instructive. Large-scale molecular simulations were conducted for crystallographic structures in the CoRE-MOF-DDEC database[43,58] to explore the potential of CO_2 physisorption for near-cryogenic DAC (Fig. 2A). Lowering the adsorption temperature strongly increases CO_2 adsorption at low CO_2 loadings (Fig. 2B).[57] The Henry's constant for CO_2 adsorption increases exponentially when the temperature is reduced from 298 K to 220 and 160 K while the heat of adsorption ($\Delta \hat{H}_s$) was largely unchanged over that same temperature range.[59] Henry's constants of promising DAC materials at room temperature were calculated to identify potential materials for near-cryogenic DAC. A heat of sorption ($\Delta \hat{H}_s$) of -60 kJ mol^{-1} has been suggested as a benchmark for DAC sorbents operating at ambient conditions.[60,61] We estimated Henry's constant at 298 K for all of the MOFs with heats of sorption around -60 kJ mol^{-1}, finding an average Henry's constant of 0.139 mol kg^{-1} Pa^{-1}. At lower temperatures, our calculations on the CoRE-MOF database materials show that this ambient temperature Henry's constant can be achieved with materials with much lower sorption enthalpies (i.e., between -40 and -24 kJ mol^{-1} for 220 and 160 K, respectively). This finding identified a large number of candidate adsorbents for DAC at near-cryogenic conditions (Fig. 2B and Fig. S2, ESI‡).

Lowering the DAC adsorption temperature reduces the gap between the optimal physical properties of DAC adsorbents and the typical properties of physisorbents (Fig. 2C). At room temperature, the properties of MOFs suitable for DAC diverge from those of most MOFs in the CoRE-MOF database. For example, most of the adsorbents predicted to be suitable for DAC at 298 K have total pore volume (V_p) between 0.249 cm^3 g^{-1} (1st quartile) and 0.346 cm^3 g^{-1} (3rd quartile), which shows minimal overlap with the total pore volume distribution of all structures in CoRE-MOF-DDEC, where the 1st and 3rd quartiles are 0.327 cm^3 g^{-1} and 0.592 cm^3 g^{-1}, respectively. However, at lower adsorption temperatures, a substantially larger fraction of the CoRE-MOF-DDEC structures—including some well-known MOFs—falls within the optimal pore volume range for DAC (Table S1, ESI‡). Similar to the total pore volume, the largest cavity diameter (LCD), crystal density (D_c) (Fig. 2C), and other physical properties (gravimetric surface area, volumetric surface area, PLD, helium void fraction, Fig. S3, ESI‡) of adsorbents for DAC application shift closer to those of most CoRE MOFs when the adsorption temperature is reduced to

220 or 160 K. This indicates that it will likely be easier to develop practical materials for near-cryogenic DAC than for DAC at ambient conditions. In addition, shifting to a larger LCD and V_p implies a higher probability of large CO_2 uptake, since adsorbents with higher LCD and V_p generally have higher saturation uptake for CO_2.[62] In particular, the peaks in the LCD range of 9.7 Å to 16.1 Å and in the V_p range of 0.73 cm^3 g^{-1} to 1.55 cm^3 g^{-1} under near-cryogenic DAC conditions highlight opportunities for very high CO_2 uptake compared with amine sorbents (Fig. S4 and S5, ESI‡). The LCD regions are also where some well-studied adsorbents are located, namely, Zeolite 13X, MIL-53(Al), HKUST-1, MOF-74(Co), and others.[63–67]

The opportunity for high CO_2 uptake in near-cryogenic DAC was explored by GCMC simulations (Fig. 2D). At 298 K, no adsorbent in the database could surpass 3 mmol g^{-1} of CO_2 uptake unless its sorption enthalpy was more exothermic than -60 kJ mol^{-1}. In contrast, many structures, especially those with sorption enthalpies between -36 and -60 kJ mol^{-1}, exhibited CO_2 uptakes exceeding 4 mmol g^{-1} at 220 K (Fig. S6, ESI‡). Based on these molecular simulations, a guideline for identifying promising materials for near-cryogenic DAC was established (Table S2, ESI‡). A search of MOF and zeolite databases using this guideline led to the selection of Zeolite 13X and CALF-20 as the most promising adsorbents, while MIL-120(Al) and Zeolite 5A also showed potential, though to a lesser extent (Fig. S7, ESI‡). We performed an experimental evaluation of these four materials.

Experimental evaluation of near-cryogenic DAC sorbents

The computational analyses described in the prior section only considered pure-CO_2 adsorption. We used experimental measurements to address the competitive adsorption of CO_2 and N_2, which is likely to be significant under near-cryogenic conditions (unlike ambient conditions). Single-component adsorption experiments were carried out with each gas and ideal adsorbed solution theory (IAST) was used to predict mixture adsorption. The first candidate, MIL-120(Al),[45] was selected because it is isostructural with MIL-120(Ga),[68] which showed high uptake at 220 K in our GCMC simulations (Fig. S8 and Table S3, ESI‡). However, experimental results revealed that MIL-120(Al) requires a temperature below 220 K to achieve sufficient CO_2 uptakes at 40 Pa (2.02 mmol g^{-1} at 180 K and 3.46 mmol g^{-1} at 160 K, Fig. 3A and Fig. S11, ESI‡). At these low temperatures, N_2 adsorption is also enhanced significantly compared to higher temperatures (Fig. S12, ESI‡). IAST calculations based on our experimental single-component data predict that N_2 is non-negligibly concentrated in the adsorbed phase on MIL-120(Al) at 160 K (Fig. 3C). The CO_2/N_2 selectivity at these conditions is predicted to be 654, which is insufficient for DAC CO_2 purity targets (>95 mol%). This example highlights the need to find materials exhibiting both high capacity for CO_2 and very high selectivity for CO_2 over N_2 under near-cryogenic conditions.

Zeolite 5A and Zeolite 13X were also selected as candidates for near-cryogenic DAC not only because their physical properties align well with the guidance established by molecular
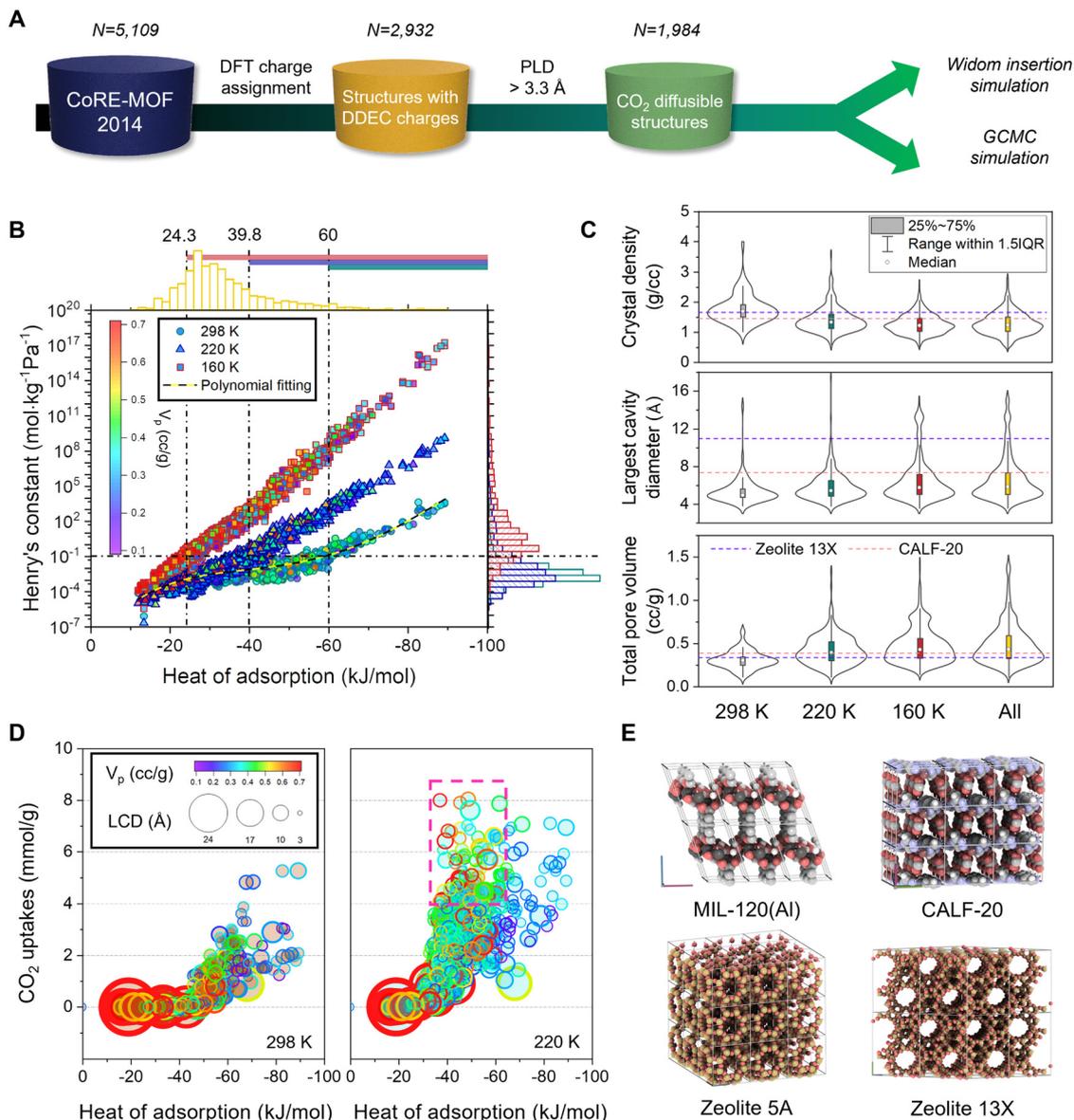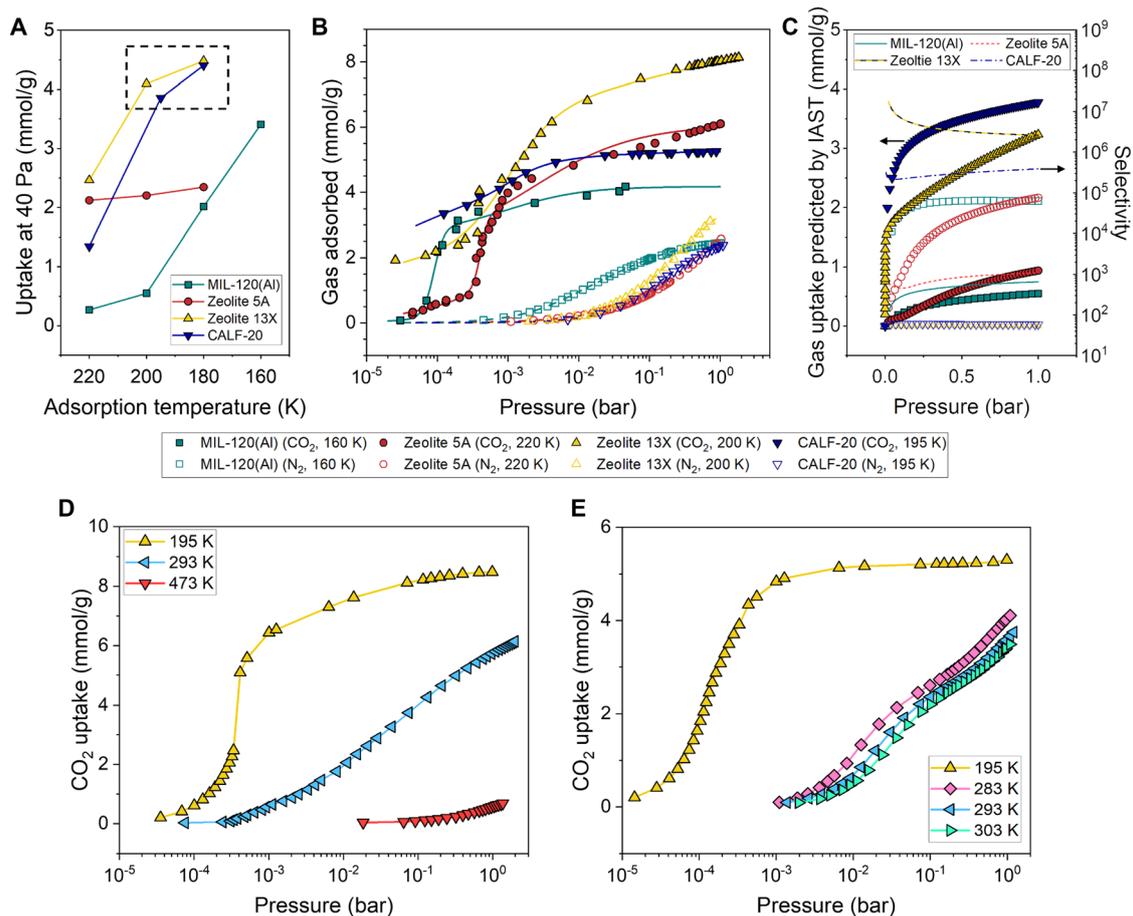
Fig. 2 Molecular simulation results for structures in the CoRE-MOF-DDEC database. (A) Dataset reduction procedure of subject structures for Widom insertion and GCMC simulations. (B) Effect of temperature on the heat and Henry's constant of CO_2 adsorption calculated from Widom insertion simulations. Each point represents a structure in the CoRE-MOF database and is color-mapped by total pore volume (V_p). The histograms on the top and right sides of the graph depict the distributions of heat of adsorption and Henry's constant for CoRE-MOFs, respectively. Red, blue, and green lines on the top histogram indicate the heat of adsorption region of candidate DAC adsorbents at 160 K, 220 K, and 298 K. (C) Violin plots of physical properties for adsorbents with suitable heats of adsorption for DAC at 160 K, 220 K, and 298 K. The suitable heat of adsorption ranges were set as $-37 < \Delta \hat{H}_s < -24$ (160 K), $-56 < \Delta \hat{H}_s < -40$ (220 K), and $-80 < \Delta \hat{H}_s < -60$ (298 K), respectively. These ranges were set to ensure the same maximum and minimum in expected Henry's constant. The properties of Zeolite 13X and CALF-20 are shown with the dashed line. (D) Effect of heats of adsorption on CO_2 uptake at 40 Pa and 298 K (left), and at 220 K (right), calculated from GCMC simulation. Each circle represents a structure in the CoRE-MOF database, and its color and size represent V_p and the largest cavity diameter (LCD). Materials showing >4 mmol g^{-1} uptake at 220 K with $\Delta \hat{H}_s$ between -36 and -60 kJ mol^{-1} are highlighted in the pink box. (E) Crystallographic structures of four candidate materials for experimental evaluation. See also Fig. S2–S8 and Tables S1 and S2 (ESI‡).

simulations (Table S2, ESI‡), but also because they are known to have strong interactions with CO_2.[69,70] Their CO_2 adsorption isotherms at 180–220 K revealed that both zeolites have significant CO_2 uptake at 40 Pa (Fig. 3A and B). However, Zeolite 5A exhibited limited CO_2/N_2 selectivity similar to MIL-120(Al), probably due to its small pore sizes, which are favorable for

N_2 (Fig. 3C). In contrast, Zeolite 13X exhibited much higher CO_2/N_2 selectivities ($\sim 10^6$) than MIL-120(Al) and Zeolite 5A. Zeolite 13X has significantly larger pore sizes (~ 10 Å) and pore volumes (0.27 cm^3 g^{-1}) than Zeolite 5A, which provides large saturation CO_2 loadings (~ 8.5 mmol g^{-1}). At 40 Pa and 200 K, Zeolite 13X utilized almost half of its large pore volume for CO_2

This journal is © The Royal Society of Chemistry 2025

Energy Environ. Sci., 2025, **18**, 7427–7439 | **7431**

Fig. 3 CO_2 adsorption isotherms from experimental measurements and IAST-predicted mixture adsorption behaviors. (A) CO_2 uptakes of MIL-120(Al), Zeolite 5A, Zeolite 13X, and CALF-20 at 40 Pa at various near-cryogenic temperatures. The dashed-line box highlights regions with promising CO_2 uptakes exceeding 3.6 mmol g^{-1}. (B) Single-component CO_2 and N_2 adsorption isotherms of MIL-120(Al) (at 160 K), Zeolite 5A (at 220 K), Zeolite 13X (at 200 K), and CALF-20 (at 195 K). The line plots represent fitted curves based on dual-site Langmuir–Freundlich equations. (C) CO_2/N_2 mixture (4/9996) adsorption isotherms and CO_2/N_2 selectivity predicted by IAST. Closed and open symbols indicate CO_2 and N_2 uptakes, respectively, while line plots represent selectivity. (D) CO_2 adsorption isotherms of Zeolite 13X at 195 K, 293 K, and 473 K. (E) CO_2 adsorption isotherms of CALF-20 at 195 K, 283 K, 293 K, and 303 K. See also Fig. S9–S14 and Table S4 (ESI‡).

adsorption (4.1 mmol g^{-1}). Notably, the adsorption capacity of Zeolite 13X observed in this study (4.1–5.5 mmol g^{-1} at 195–200 K) is nearly double the previously reported performance at cold sub-ambient temperatures ($\sim$2.8 mmol g^{-1} at 215 K),[24] further emphasizing the advantages of near-cryogenic DAC. CO_2 equilibrium uptake of Zeolite 13X at 473 K and 1 bar was 0.56 mmol g^{-1} (Fig. 3D), indicating low residual CO_2 loading under desorption with high-purity CO_2 sweep gas, which in turn leads to a high CO_2 working capacity.

CALF-20, a MOF of considerable interest due to its promising CO_2 adsorption behavior, scalable synthesis, and long-term stability even under steam desorption conditions,[47] also demonstrated significant CO_2 sorption capacity at 195 K ($\sim$4.3 mmol g^{-1}, Fig. 3B and E). This observation is particularly surprising, considering that CALF-20 had previously shown negligible CO_2 sorption ($<$0.1 mmol g^{-1}) from DAC-level dilute CO_2 sources at room temperature.[20] IAST results indicated that CALF-20 adsorbs CO_2 almost exclusively over N_2 at 195 K, with a CO_2/N_2 adsorption selectivity exceeding 4×10^5, well beyond the requirements for DAC

purity targets. At near room temperature (283–303 K), CALF-20 exhibited low CO_2 uptakes, consistent with previous observations of its desorbability under mild conditions.[71] These characteristics suggest potential use of CALF-20 for vacuum-assisted desorption under near-room temperatures (Fig. 3E). Given their performance under near-cryogenic DAC conditions, scalability, and long-term stability, Zeolite 13X and CALF-20 were selected for further mixture adsorption testing using dynamic breakthrough analysis.

Dynamic breakthrough analysis on Zeolite 13X and CALF-20 powder columns was performed at 195 K using a dry ice/ethanol cooling bath (Fig. 4 and Fig. S15, ESI‡). The Zeolite 13X powder-packed bed exhibited highly favorable DAC performance: we observed approximately 5.5 mmol g^{-1} of CO_2 pseudo-equilibrium capacity under a 100 sccm flow of a 400 ppm CO_2 mixture balanced with N_2 (Fig. 4A). The capacity aligns well with single-component CO_2 uptake of Zeolite 13X at 40 Pa and 195 K (Fig. 3D and Fig. S16, ESI‡), consistent with exceptionally high CO_2/N_2 selectivity from IAST. The high pseudo-equilibrium capacity was also observed at the higher
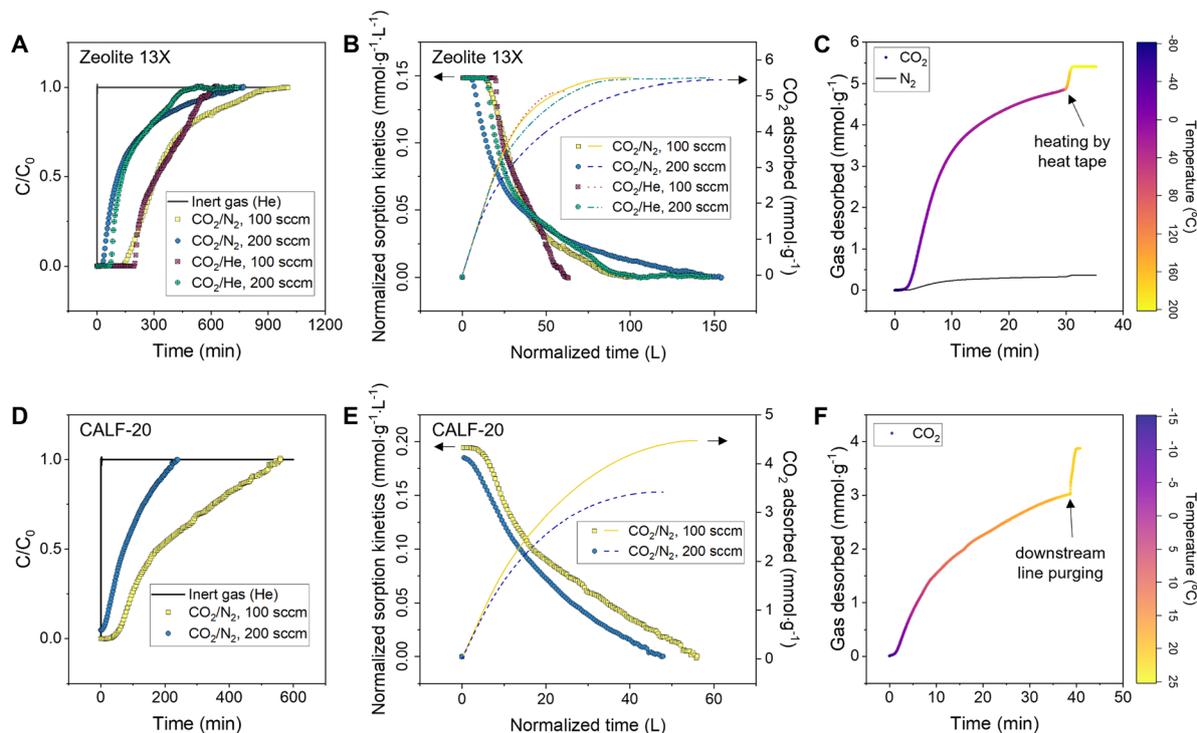
Fig. 4 Dynamic breakthrough analysis of powder-packed Zeolite 13X and CALF-20 bed at 195 K. (A) Breakthrough curves and (B) corresponding CO_2 adsorption kinetics of powder-packed Zeolite 13X bed under a CO_2 (400 ppm)/N_2 (balance) feed mixture and under a CO_2 (400 ppm)/He (balance) mixture. (C) Integral desorption profile of the Zeolite 13X bed under He flow at 200 °C. (D) Breakthrough curves and (E) CO_2 adsorption kinetics of powder-packed CALF-20 bed under a CO_2 (400 ppm)/N_2 (balance) mixture. The 200 sccm data were obtained after degassing at 22 °C and 0.08 bar. (F) Integral desorption profile of the CALF-20 bed by applying vacuum at 22 °C. See also Fig. S17–S21 (ESI‡). Normalized time (L) is defined as the product of time and flow rate (L = time × flow rate).

flow rate of 200 sccm (Fig. 4A), indicating that the system is not strongly limited by adsorption kinetics even at low temperatures within this flow regime. However, when the CO_2 breakthrough curves measured under a CO_2 (400 ppm)/N_2 (balance) feed mixture were compared to those under a CO_2 (400 ppm)/He (balance) mixture, the curves were less sharp and exhibited broader mass transport zones (Fig. 4A and B). This effect became more pronounced at the 200 sccm flow rate, where the adsorption speed under a He balance was much faster than under an N_2 balance, implying slower adsorption kinetics in the N_2 atmospheres, as expected given the relative magnitudes of CO_2–He and CO_2–N_2 gas–gas diffusivities. Overall, the results indicate the presence of some competitive adsorption kinetic limitations at 195 K. We were able to close the mass balance and observed that the adsorbed CO_2 could be recovered almost fully by heating the bed up to 200 °C while flowing He (Fig. 4C). The purity of the desorbed gas was high (94%) despite the probable presence of some N_2 in the interstitial volume of the column after the initial He sweep.
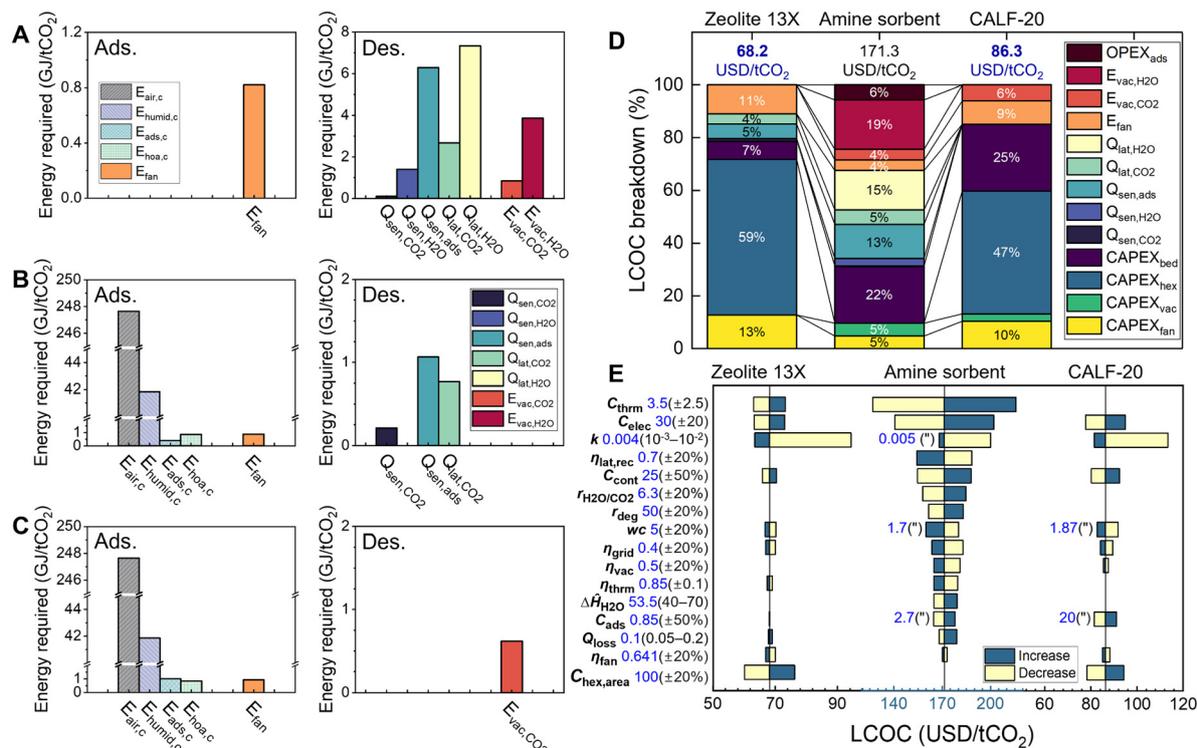
CALF-20 also exhibited a large pseudo-equilibrium capacity of 4.5 mmol g^{-1} under a 100 sccm flow of a 400 ppm CO_2 mixture balanced with N_2 at 195 K (Fig. 4D and E). Considering the sample amount in the fixed bed and CO_2 uptakes, the overall sorption kinetics of Zeolite 13X and CALF-20 were comparable under a flow rate of 100 sccm (Fig. S21, ESI‡). After the first

adsorption cycle, the column was exposed to a vacuum of approximately 0.08 bar while being heated to 22 °C (Fig. 4F). Desorbed CO_2 under the near–room–temperature desorption was quantified as 3.9 mmol g^{-1}, highlighting the feasibility of CALF-20 desorption at low temperatures. A second adsorption cycle was conducted under a 200 sccm flow of a 400 ppm CO_2 mixture balanced with N_2, which resulted in a pseudo-equilibrium capacity of 3.4 mmol g^{-1}—around 76% of the adsorbed CO_2 during the initial adsorption (Fig. 4E). The slight discrepancy between the regenerated CO_2 capacity and the quantified desorbed CO_2 may be attributed to inaccuracies in quantifying CO_2 residue within the downstream lines and the internal pump volume. Zeolite 13X and CALF-20 exhibited no observable decrease in CO_2 uptake over ten cycles of near-cryogenic adsorption and desorption, indicating that their well-established stability also holds under cryogenic DAC conditions (Fig. S22, ESI‡).[47,72,73]

Techno-economic analysis of the near-cryogenic DAC process

Based on the experimental results, the thermal and electrical energy requirements for the near-cryogenic DAC using Zeolite 13X and CALF-20 were estimated and compared with those of ambient DAC using an amine sorbent (Fig. 5A–C). For the cost model, CO_2 uptake under near-cryogenic conditions was taken from dynamic breakthrough experiments using a 400 ppm CO_2/N_2 mixture, while the residual CO_2 under desorption conditions

This journal is © The Royal Society of Chemistry 2025

Energy Environ. Sci., 2025, **18**, 7427–7439 | **7433**

Fig. 5 Energy requirement and cost estimation for LNG–DAC. Thermal and electrical energy requirements during adsorption (left) and desorption (right) for (A) ambient DAC with an amine sorbent using temperature-vacuum swing, (B) near-cryogenic DAC with Zeolite 13X, using high-purity CO_2 as a sweep gas for desorption, and (C) near-cryogenic DAC with CALF-20 utilizing ambient-temperature desorption with the aid of a vacuum swing. Refer to Table 1 for the list of symbols. (D) Breakdown of levelized cost of capture (LCOC) for LNG–DAC with Zeolite 13X, LNG–DAC with CALF-20, and ambient DAC with an amine sorbent. (E) Parametric sensitivity analysis of LCOC for the three processes. The parameter ranges are shown on the left-hand side unless specified alongside individual bars. C_{thrm}: thermal energy unit cost (USD per GJ), C_{elec}: electrical energy unit cost (USD per MWh), k: overall mass transfer coefficient (m s^{-1}), $\eta_{lat,rec}$: water latent heat recovery efficiency, C_{cont}: contactor base cost (USD per kg_{ads}), r_{H_2O/CO_2}: H_2O/CO_2 selectivity (kg kg^{-1}), r_{deg}: Annual degradation rate (%/year), wc: CO_2 working capacity (mmol g^{-1}), η_{grid}: electrical energy efficiency, η_{vac}: vacuum efficiency, η_{thrm}: thermal energy efficiency, $\Delta \dot{H}_{s,H_2O}$: heat of water adsorption (kJ mol^{-1}), C_{ads}: Sorbent base price (USD per kg), Q_{loss}: heat loss, η_{fan}: fan efficiency, $C_{hex,area}$: heat exchanger unit cost (USD per m^2). See also Fig. S23–S28 and Tables S5–S10 (ESI‡).

was taken from single-component isotherms, assuming near-equilibrium behavior due to elevated temperature and a CO_2-rich environment (Tables S8 and S9, ESI‡). Unlike the ambient DAC process, which requires only fan energy (E_{fan}) during adsorption, the near-cryogenic DAC process demands significant amounts of cold energy, mainly for cooling down ($E_{air,c}$ = 247.6 GJ per tCO_2) and dehumidifying ($E_{humid,c}$ = 41.8 GJ per tCO_2) atmospheric air at the global average temperature (14–15 °C) (Fig. 5B and C). Providing cold energy at such a scale through an external cooling cycle is economically prohibitive, making coupling with LNG regasification essential unless the process is conducted in very cold climates (Fig. S23, ESI‡). In the LNG–DAC process, the cold energy from LNG regasification (290.4 GJ per tCO_2) compensates for all four thermal energy requirements during the adsorption process, namely, $E_{air,c}$, $E_{humid,c}$, $E_{ads,c}$ (energy for cooling adsorbents), and $E_{hoa,c}$ (heats of adsorption). To meet these significant cold energy demands, 327.9 tons of LNG must be regasified per ton of CO_2 captured, which implies a potential limitation on scale due to the availability of LNG resources. However, with advancements in adsorbent materials and process

design—which are discussed in detail in the final two paragraphs of the Results and Discussion section, including cold energy recovery from the cold downstream air[25,26]—LNG consumption could decrease to 30.1 tLNG per tCO_2 (See also sections S3.5–S3.6 in ESI‡). Aside from the cold energy, adsorption under near-cryogenic conditions incurs a slightly higher E_{fan} owing to less efficient mass transport at these temperatures (Tables S7–S9, ESI‡).

Near-cryogenic DAC demonstrated significant energy savings in the desorption process compared to ambient DAC (Fig. 5A–C). The energy requirements of ambient DAC using amine sorbents were estimated assuming an annual sorbent degradation rate of 50% and 70–90% recovery of water latent heat.[14] The results indicate that the conventional temperature-vacuum adsorption (TVSA) process with amine sorbents can require substantial thermal energy (12.9–17.8 GJ per tCO_2) and electrical energy (5.5 GJ per tCO_2). The energy associated with water desorption (Q_{sen,H_2O}, Q_{lat,H_2O}, and E_{vac,H_2O}) is a significant contributor, accounting for 42–54% of the total energy consumption. When sorbent degradation is assumed to be negligible, the thermal energy requirements were 9.1–14 GJ per

7434 | *Energy Environ. Sci.*, 2025, **18**, 7427–7439

This journal is © The Royal Society of Chemistry 2025

Table 1 Components of energy duty and levelized cost of capture breakdown

Parameter	Description	Parameter	Description
Energy duties and OPEX in levelized cost of capture (LCOC)			
$E_{air,c}$	Cold energy for dry air cooling	Q_{sen,H_2O}	Sensible heat for H_2O
$E_{humid,c}$	Cold energy for humidity removal	Q_{sen,CO_2}	Sensible heat for CO_2
$E_{ads,c}$	Cold energy for sorbent cooling	Q_{lat,H_2O}	Latent heat for H_2O
$E_{hoa,c}$	Cold energy for adsorption heat removal	Q_{lat,CO_2}	Latent heat for CO_2
E_{fan}	Electrical energy for fan	$Q_{sen,ads}$	Sensible heat for adsorbent
E_{vac,CO_2}	Electrical energy for vacuuming CO_2	$OPEX_{ads}$	Sorbent replacement cost
E_{vac,H_2O}	Electrical energy for vacuuming H_2O		
CAPEX in LCOC			
$CAPEX_{bed}$	Capital expenditure for sorbent bed	$CAPEX_{vac}$	Capital expenditure for vacuum pump
$CAPEX_{hex}$	Capital expenditure for heat exchanger	$CAPEX_{fan}$	Capital expenditure for fan

tCO_2, which is comparable to previous studies.[16,74] We note that these energy requirements can likely be decreased *via* improved materials (especially water : CO_2 sorption ratios) and heat integration.

In contrast, the LNG–DAC process eliminates the water-related energy costs to the DAC plant operator. Additionally, when using Zeolite 13X, employing high-purity CO_2 as a sweep gas further reduces desorption energy consumption and complexity by eliminating the need for vacuum pump operation (Fig. 5B). After accounting for the energies compensated by heat exchange with seawater during bed heating step, the thermal energy input required for desorption was 2.0 GJ per $tCO_{2,RE}$. These low thermal energy requirements are also attributed to the advantages of physisorbents in working capacity, heat of adsorption,[75] and specific heat capacity of sorbents.[76] Considering CO_2 emissions from thermal energy production *via* NG combustion for process operations, the overall energy requirement for adsorption and desorption of the Zeolite 13X system amounts to 3.3 GJ per $tCO_{2,NRE}$.

The near-cryogenic DAC with CALF-20 was designed to perform desorption at ambient temperature (283 K), which can be achieved through heat exchange with seawater or other low-grade heat sources. As a result, the CALF-20 system requires no additional thermal energy input for desorption and relies exclusively on electrical energy for vacuum pump and fan operation (Fig. 5C). In terms of energy efficiency, the CALF-20 system outperformed the Zeolite 13X system, with a total energy requirement of 1.7 GJ per $tCO_{2,NRE}$.

Finally, the levelized cost of capture (LCOC) for near-cryogenic DAC was evaluated compared to ambient DAC (Fig. 5D). For a conventional ambient DAC using amine sorbents, the primary contributors to the LCOC (171.3 USD per $tCO_{2,RE}$) are the energy costs associated with managing water co-adsorbed with CO_2 (35% of LCOC) and the costs related to the sorbent contactor, including $OPEX_{ads}$ (5.6%), $CAPEX_{cont}$ (19.3%), and $Q_{sen,ads}$ (12.8%). The water-related components of the LCOC are primarily influenced by sorbent material parameters such as the ratio of CO_2 working capacity to water working capacity (r_{H_2O/CO_2}), the heat of water adsorption ($\Delta\hat{H}_{s,amine,H_2O}$), and the recovery efficiency of water latent heat ($\eta_{lat,rec}$) (Fig. 5E). Other main contributors, $OPEX_{ads}$, $CAPEX_{cont}$, and $Q_{sen,ads}$ are largely dependent on factors such as annual sorbent degradation (r_{deg}), contactor cost (C_{cont}), and CO_2

working capacity (wc).[13,14] The integration with renewable energy is critical for achieving cost-efficient DAC with amine sorbents, as the use of NG combustion leads to a high LCOC of 1231.7 USD per $tCO_{2,NRE}$.

The near-cryogenic DAC process provides significant improvements in all the main cost-driving parameters identified in conventional DAC (Fig. 5D). Zeolite 13X system achieves large cost reductions by eliminating water desorption-related expenses and vacuum energy costs. In addition, it shows improvement in $OPEX_{ads}$, $CAPEX_{cont}$, and $Q_{sen,ads}$ from amine sorbent-based system due to enhanced sorbent characteristics, including wc (1.7 mmol g^{-1} → 5 mmol g^{-1}) and r_{deg} (0.5 → 0). It is notable that the cost saving comes at the expense of substantial investment in additional heat exchange area required for thermal coupling between LNG regasification and DAC (Fig. S25–S28, ESI‡). Overall, the LNG–DAC process with Zeolite 13X is projected to reduce the LCOC by approximately 60%, achieving low-cost DAC at 68.2 USD per $tCO_{2,RE}$.

The LNG–DAC process with CALF-20 also demonstrates a promising LCOC (86.3 USD per $tCO_{2,RE}$) by eliminating water desorption-related costs and thermal energy costs. The main contributor to the higher LCOC compared to the Zeolite 13X system is the significantly higher $CAPEX_{ads}$, resulting from the higher sorbent cost (C_{ads}, 20 USD per kg) of CALF-20 and its lower wc (1.8 mmol g^{-1}) due to low desorption temperature. That said, the relative economic feasibility of the Zeolite 13X and CALF-20 systems may vary depending on the prices of thermal and electrical energy (C_{elec} and C_{thrm}) and their efficiencies (η_{grid} and η_{thrm}) (Fig. 5E). Notably, due to the minor cost contribution of thermal energy demand, both the Zeolite 13X and CALF-20 systems exhibited much smaller increases in LCOC when assuming NG combustion as the source of thermal energy (78.9 USD per $tCO_{2,NRE}$ and 86.8 USD per $tCO_{2,NRE}$, respectively).

Overall, the near-cryogenic DAC consistently outperforms the amine sorbent-based system under most scenarios. The cost effectiveness of the two processes becomes comparable only when the five key parameters—mass transfer coefficient (k), heat exchanger unit cost ($C_{hex,area}$), wc, C_{elec}, and C_{thrm}—are simultaneously set to favor the ambient DAC system and disadvantage the near-cryogenic DAC system (Fig. 5E and Fig. S29, ESI‡). Relative to typical DAC systems, the LNG–DAC system may require a 13–27% increase in land footprint due to

the volume of additional heat exchangers. However, this may be partially offset by a reduced vaporizer volume required at the regasification terminal.

We explored the global carbon drawdown potential of the LNG–DAC concept. Without cold energy recovery, the global deployment of LNG–DAC is projected to be constrained to only 4.2 MTPA and 6.6 MTPA, based on current global LNG regasification capacity and projections for 2050, respectively (Fig. S28, ESI‡).[77,78] This highlights the need for investment in air–air heat exchangers for cold energy recovery is critical to extending the long-term impact of LNG–DAC, which has already been accounted for in the techno-economic analysis (Fig. 5). The recovery efficiency of cold energy from downstream cold air is assumed to reach 0.9 as of 2050, as proposed in earlier cryogenic DAC studies.[25,26] Another frequently considered process combination in carbon capture involves blending feed air with CO_2 emissions from natural gas combustion, which provides thermal energy for the process. This integration can lower total cold energy consumption by approximately 12.5% (Fig. S28, ESI‡). Given the relatively uncommon adsorption conditions of near-cryogenic DAC, there is substantial potential to develop advanced sorbents that achieve high capture efficiency ($\sim$0.9) at relatively high temperatures ($\sim$240 K), thereby reducing the LNG/CO_2 ratio further (Fig. S30 and S31, ESI‡).

Considering these potential advancements, along with the emergence of cold energy resources from hydrogen and ammonia economies,[77,79] the global LNG–DAC potential could reach 44–45 MTPA by 2030 and 103–142 MTPA by 2050, depending on LNG regasification growth (Fig. S32, ESI‡). This would account for approximately 10.6–14.6% of the overall DAC target for 2050 (970 MTPA),[80] indicating that LNG–DAC has the potential to substantially contribute to both short- and long-term DAC objectives as a negative emission technology.

Conclusion

DAC at near-cryogenic temperatures makes it possible to unlock the full potential of large-pore-volume physisorbents, offering exceptionally high CO_2 working capacity with lower desorption enthalpy. For example, Zeolite 13X exhibits nearly double the sorption capacity under DAC conditions at 195 K compared to the coldest sub-ambient DAC system in polar regions (215 K), underscoring the advantages of operating at lower temperatures. Performing DAC at near-cryogenic conditions, of course, requires energy input associated with achieving the relevant temperatures. The energy required for near-cryogenic DAC when performed *via* thermal coupling with LNG regasification can be as low as 1.7–3.3 GJ per tCO_2. As a result, the levelized cost of capture (LCOC) for near-cryogenic DAC is estimated to be approximately half that of state-of-the-art amine sorbent-based systems. Near-cryogenic DAC also offers considerable potential for further energy efficiency improvements through integration with green processes such as Rankine cycles, air separation units (ASU), and hydrogen or ammonia production.

We used molecular simulations to demonstrate that near-cryogenic DAC offers an opportunity to employ a broad range of physisorbents. Zeolite 13X stands out as a promising candidate with a high CO_2 capacity of 5.5 mmol g^{-1} at 195 K. Similarly, CALF-20, despite underperforming in ambient or sub-ambient DAC conditions, achieves a CO_2 capacity of 4.5 mmol g^{-1} at 195 K. Beyond their high CO_2 capacities, both sorbents exhibit critical characteristics such as low desorption enthalpy, cost efficiency, scalability, and long-term stability, all of which are essential for real-world applications. Based on simulation results, sorbents with heat of adsorption between −36 kJ mol^{-1} and −60 kJ mol^{-1} should be prioritized for evaluating their DAC potential at near-cryogenic temperatures. The development of advanced sorbent materials could further reduce the cost of the near-cryogenic DAC process beyond the estimates presented in this study.

The adsorption behavior of CALF-20 introduces an intriguing concept: a temperature swing from near-cryogenic conditions to room temperature, relying solely on low-grade heat energy (*e.g.*, heat exchange with seawater). CALF-20 exhibited a moderate CO_2 swing capacity between adsorption from 400 ppm CO_2 mixture at 195 K and desorption at 283 K under vacuum. Our analysis indicates that the LCOC of the CALF-20-based system exceeds that of the Zeolite 13X-based system that requires external thermal energy input; however, their relative cost-effectiveness could shift depending on factors such as the prices of thermal and electrical energy.

Key limitations of this study include a relatively modest analysis of the adsorption kinetics under near-cryogenic conditions. While we observed no major kinetic limitations within a narrow window of air velocities, the kinetics at higher velocities require further examination. That said, even under the assumption of a lower mass transfer coefficient, near-cryogenic DAC demonstrates a lower LCOC.

Another limitation lies in the estimation of the potential scale of the LNG–DAC process, given its reliance on the forecasts for global LNG resources and the potential development of sorbents. Still, near-cryogenic DAC *via* LNG–DAC coupling could drive early DAC deployment, which is increasingly recognized as critical for influencing global temperature trajectories.[81,82] Its potential scale could cover approximately 60% of the DAC target as of 2030. The potential upper limit of the LNG–DAC process's contribution to net zero emissions is estimated to be 11–15% of the DAC target as of 2050, depending on the capture efficiency of sorbent materials. The significant cost reduction ($\sim$60%) compared to conventional amine sorbent-based systems, however, makes including LNG–DAC in the DAC portfolio impactful even with a limited share.

Methods

Widom insertion and GCMC simulations were conducted for CoRE-MOF-DDEC database[58] using RASPA2.0.[83] The LJ parameters of framework atoms were assigned following the UFF forcefield.[84] The TraPPE model[85] was used for adsorbate molecules.

7436 | *Energy Environ. Sci.*, 2025, **18**, 7427–7439

This journal is © The Royal Society of Chemistry 2025

Physical properties of crystallographic structures were determined by Zeo++ package.[86] Detailed simulation procedures are presented in Section S1 in ESI.‡

MIL-120(Al) and CALF-20 were synthesized following previously reported procedures.[45,87] Zeolite 13X and Zeolite 5A were purchased from MilliporeSigma (US) and used without further treatment. CO_2 and N_2 adsorption isotherms at near-cryogenic temperatures were measured using HPVA II with a single-stage cryogenic refrigerator, Cryostat I (Micromeritics Instrument Corporation, US). IAST predictions were conducted using the IAST++ software[88] by fitting the experimental data to the dual-site Langmuir–Freundlich equation. CO_2 adsorption behaviors of Zeolite 13X and CALF-20 were also measured in a volumetric apparatus capable of activation under high vacuum, ASAP2020HD analyzer (Micromeritics Instrument Corporation, US) using a dry ice/acetone cooling bath.

The breakthrough analyses of Zeolite 13X and CALF-20 were conducted at 195 K using a custom-built fixed bed system (Fig. S15, ESI‡). The powder sample was loosely packed in a 10 cm long, 1/4 inch stainless steel tube. The temperature was held around 195 K via a dry ice/ethanol cooling bath. The outlet gas concentration profile was recorded by LI-850 gas analyzer (LI-COR Biosciences, USA) or Pfeiffer Vacuum QMS 200 Omnistar Mass Spectrometer (Pfeiffer Vacuum GmbH, Germany). Detailed experimental procedures are presented in Section S2 in ESI.‡

Energy duty estimation and techno-economic analysis for near-cryogenic DAC and ambient DAC, LNG–DAC potential scale estimation, and energy duty estimation for near-cryogenic DAC with external cooling cycles,[25] were described in detail in Section S3 in ESI.‡

Author contributions

Conceptualization, S. K.; methodology, S. K. and R. P. L.; investigation, S. K. and A. S.; formal analysis, S. K.; writing – original draft, S. K.; writing – review & editing, S. K., A. S., S. C., J. K., M. J. R., D. S. S., and R. P. L.; funding acquisition, R. P. L.; resources, D. S. S. and R. P. L.; supervision, R. P. L.

Conflicts of interest

The authors declare no competing interests. Georgia Tech Research Corporation has applied for provisional disclosure for the processes discussed herein, on which S. K. and R. P. L. are included as inventors.

Data availability

The data supporting this article have been included as part of the ESI.‡

Acknowledgements

References

1 S. Chowdhury, Y. Kumar, S. Shrivastava, S. K. Patel and J. S. Sangwai, *Energy Fuels*, 2023, **37**, 10733–10757.

2 J. Fuhrman, A. Clarens, K. Calvin, S. C. Doney, J. A. Edmonds, P. O'Rourke, P. Patel, S. Pradhan, W. Shobe and H. McJeon, *Environ. Res. Lett.*, 2021, **16**, 114012.

3 W. H. Lee, X. Zhang, S. Banerjee, C. W. Jones, M. J. Realff and R. P. Lively, *Joule*, 2023, **7**, 1241–1259.

4 X. Zhu, W. Xie, J. Wu, Y. Miao, C. Xiang, C. Chen, B. Ge, Z. Gan, F. Yang, M. Zhang, D. O'Hare, J. Li, T. Ge and R. Wang, *Chem. Soc. Rev.*, 2022, **51**, 6574–6651.

5 E. S. Sanz-Pérez, C. R. Murdock, S. A. Didas and C. W. Jones, *Chem. Rev.*, 2016, **116**, 11840–11876.

6 R. Hanna, A. Abdulla, Y. Xu and D. G. Victor, *Nat. Commun.*, 2021, **12**, 368.

7 J. Rogelj, A. Popp, K. V. Calvin, G. Luderer, J. Emmerling, D. Gernaat, S. Fujimori, J. Strefler, T. Hasegawa, G. Marangoni, V. Krey, E. Kriegler, K. Riahi, D. P. van Vuuren, J. Doelman, L. Drouet, J. Edmonds, O. Fricko, M. Harmsen, P. Havlík, F. Humpenöder, E. Stehfest and M. Tavoni, *Nat. Clim. Change*, 2018, **8**, 325–332.

8 G. Realmonte, L. Drouet, A. Gambhir, J. Glynn, A. Hawkes, A. C. Köberle and M. Tavoni, *Nat. Commun.*, 2019, **10**, 3277.

9 F. Sabatino, A. Grimm, F. Gallucci, M. van Sint Annaland, G. J. Kramer and M. Gazzani, *Joule*, 2021, **5**, 2047–2076.

10 K. Sievert, T. S. Schmidt and B. Steffen, *Joule*, 2024, **8**, 979–999.

11 L. Küng, S. Aeschlimann, C. Charalambous, F. McIlwaine, J. Young, N. Shannon, K. Strassel, C. N. Maesano, R. Kahsar, D. Pike, M. van der Spek and S. Garcia, *Energy Environ. Sci.*, 2023, **16**, 4280–4304.

12 J. Young, N. McQueen, C. Charalambous, S. Foteinis, O. Hawrot, M. Ojeda, H. Pilorgé, J. Andresen, P. Psarras, P. Renforth, S. Garcia and M. van der Spek, *One Earth*, 2023, **6**, 899–917.

13 N. McQueen, K. V. Gomes, C. McCormick, K. Blumanthal, M. Pisciotta and J. Wilcox, *Prog. Energy*, 2021, **3**, 032001.

14 H. E. Holmes, S. Banerjee, A. Vallace, R. P. Lively, C. W. Jones and M. J. Realff, *Energy Environ. Sci.*, 2024, **17**, 4544–4559.

15 S. Deutz and A. Bardow, *Nat. Energy*, 2021, **6**, 203–213.

16 K. An, K. Li, C.-M. Yang, J. Brechtl and K. Nawaz, *J. CO2 Util.*, 2023, **76**, 102587.

17 H. E. Holmes, R. P. Lively and M. J. Realff, *JACS Au*, 2021, **1**, 795–806.

18 X. Shi, H. Xiao, H. Azarabadi, J. Song, X. Wu, X. Chen and K. S. Lackner, *Angew. Chem., Int. Ed.*, 2020, **59**, 6984–7006.

19 M. Ding, R. W. Flaig, H.-L. Jiang and O. M. Yaghi, *Chem. Soc. Rev.*, 2019, **48**, 2783–2828.

20 S. Bose, D. Sengupta, T. M. Rayder, X. Wang, K. O. Kirlikovali, A. K. Sekizkardes, T. Islamoglu and O. K. Farha, *Adv. Funct. Mater.*, 2023, **34**, 2307478.

21 S. Mahajan and M. Lahtinen, *J. Environ. Chem. Eng.*, 2022, **10**, 108930.

22 L. Jiang, R. Y. Xie, W. K. Shi, E. Y. Wu, B. Li and X. J. Zhang, *Carbon Capture Sci. Technol.*, 2022, **4**, 100061.

This journal is © The Royal Society of Chemistry 2025

Energy Environ. Sci., 2025, **18**, 7427–7439 | 7437

23 M. Song, G. Rim, F. Kong, P. Priyadarshini, C. Rosu, R. P. Lively and C. W. Jones, *Ind. Eng. Chem. Res.*, 2022, **61**, 13624–13634.

24 S. M. W. Wilson, *iScience*, 2022, **25**, 105564.

25 S. K. S. Boetcher, J. B. Perskin, Y. Maidenberg, M. J. Traum and T. von Hippel, *Carbon Capture Sci. Technol.*, 2023, **8**, 100127.

26 S. K. S. Boetcher, M. J. Traum and T. von Hippel, *Clim. Change*, 2020, **158**, 517–530.

27 J. F. Wiegner, A. Grimm, L. Weimann and M. Gazzani, *Ind. Eng. Chem. Res.*, 2022, **61**, 12649–12667.

28 J. Kim, J. Park, M. Qi, I. Lee and I. Moon, *Ind. Eng. Chem. Res.*, 2021, **60**, 7257–7274.

29 R. Agarwal, T. J. Rainey, S. M. A. Rahman, T. Steinberg, R. K. Perrons and R. J. Brown, *Energies*, 2017, **10**, 2152.

30 T. Sung and K. C. Kim, in *Energy Solutions to Combat Global Warming*, ed. X. Zhang and I. Dincer, Springer, Cham, 2017, 33, ch. LNG Cold Energy Utilization Technology, pp. 47–66.

31 R. Ferreiro García, J. Carbia Carril, J. Romero Gomez and M. Romero Gomez, *Energy Convers. Manage.*, 2015, **101**, 285–294.

32 P. Dorosz, P. Wojcieszak and Z. Malecha, *Entropy*, 2018, **20**, 59.

33 D. Kim, R. E. H. Giametta and T. Gundersen, *Ind. Eng. Chem. Res.*, 2018, **57**, 5914–5923.

34 S.-Y. Kim, S. Han, S. Lee, J. H. Kang, S. Yoon, W. Park, M. W. Shin, J. Kim, Y. G. Chung and Y.-S. Bae, *Adv. Sci.*, 2022, **9**, 2201559.

35 E. A. Roszak and M. Chorowski, *AIP Conf. Proc.*, 2014, **1573**, 1379–1386.

36 Y. Kim, J. Lee, N. An and J. Kim, *Energy Convers. Manage.*, 2023, **292**, 117349.

37 H. Yu, T. Gundersen and E. Gençer, *Energy Convers. Manage.*, 2021, **228**, 113725.

38 L. F. A. S. Zafanelli, E. Aly, A. E. Rodrigues and J. A. C. Silva, *Sep. Purif. Technol.*, 2023, **307**, 122824.

39 M. A. Moreira, A. M. Ribeiro, A. F. P. Ferreira and A. E. Rodrigues, *Sep. Purif. Technol.*, 2017, **173**, 339–356.

40 S. J. A. DeWitt, R. Awati, H. Octavio Rubiera Landa, J. Park, Y. Kawajiri, D. S. Sholl, M. J. Realff and R. P. Lively, *AIChE J.*, 2021, **67**, e17403.

41 T. Banaszkiewicz, *Entropy*, 2021, **23**, 350.

42 C. A. Grande and R. Blom, *Energy Fuels*, 2014, **28**, 6688–6693.

43 T. A. Manz and D. S. Sholl, *J. Chem. Theory Comput.*, 2010, **6**, 2455–2468.

44 S.-Y. Kim, S.-I. Kim and Y.-S. Bae, *J. Phys. Chem. C*, 2020, **124**, 19538–19547.

45 C. Volkringer, T. Loiseau, M. Haouas, F. Taulelle, D. Popov, M. Burghammer, C. Riekel, C. Zlotea, F. Cuevas, M. Latroche, D. Phanon, C. Knöfelv, P. L. Llewellyn and G. Férey, *Chem. Mater.*, 2009, **21**, 5783–5791.

46 S. Ahsan, A. Ayub, D. Meeroff and M. Jahandar Lashaki, *Chem. Eng. J.*, 2022, **437**, 135139.

47 J.-B. Lin, T. T. T. Nguyen, R. Vaidhyanathan, J. Burner, J. M. Taylor, H. Durekova, F. Akhtar, R. K. Mah, O. Ghaffari-Nik, S. Marx, N. Fylstra, S. S. Iremonger, K. W. Dawson, P. Sarkar, P. Hovington, A. Rajendran, T. K. Woo and G. K. H. Shimizu, *Science*, 2021, **374**, 1464–1469.

48 E. A. Roszak and M. Chorowski, *AIP Conf. Proc.*, 2012, **1434**, 1771–1778.

49 A. Salem and E. Hudiab, *Int. J. Energy*, 2014, 84–90.

50 V. L. Bondarenko and T. V. D'yachenko, *Chem. Pet. Eng.*, 2020, **56**, 255–262.

51 R. E. Bernert, W. Everett and R. E. Bernert, *Cryogenics*, 1993, **33**, 789–793.

52 M. Mehrpooya, M. Kalhorzadeh and M. Chahartaghi, *J. Cleaner Prod.*, 2016, **113**, 411–425.

53 R. Peeters, H. Vanderschaeghe, J. Rongé and J. A. Martens, *iScience*, 2021, **24**, 103266.

54 M. Babar, M. Mubashir, A. Mukhtar, S. Saqib, S. Ullah, M. A. Bustam and P. L. Show, *Environ. Pollut.*, 2021, **279**, 116924.

55 P. M. Bhatt, Y. Belmabkhout, A. Cadiau, K. Adil, O. Shekhah, A. Shkurenko, L. J. Barbour and M. Eddaoudi, *J. Am. Chem. Soc.*, 2016, **138**, 9301–9307.

56 E. Moubarak, S. M. Moosavi, C. Charalambous, S. Garcia and B. Smit, *Ind. Eng. Chem. Res.*, 2023, **62**, 10252–10265.

57 J. M. Findley and D. S. Sholl, *J. Phys. Chem. C*, 2021, **125**, 24630–24639.

58 D. Nazarian, J. S. Camp and D. S. Sholl, *Chem. Mater.*, 2016, **28**, 785–793.

59 D. V. Cao and S. Sircar, *Adsorpt. Sci. Technol.*, 2001, **19**, 887–894.

60 R. P. Lively and M. J. Realff, *AIChE J.*, 2016, **62**, 3699–3705.

61 M.-Y. Low, L. V. Barton, R. Pini and C. Petit, *Chem. Eng. Res. Des.*, 2023, **189**, 745–767.

62 X. Zhang, R.-B. Lin, J. Wang, B. Wang, B. Liang, T. Yildirim, J. Zhang, W. Zhou and B. Chen, *Adv. Mater.*, 2020, **32**, 1907995.

63 B. Chen, N. W. Ockwig, A. R. Millward, D. S. Contreras and O. M. Yaghi, *Angew. Chem., Int. Ed.*, 2005, **44**, 4745–4749.

64 C. H. Hendon and A. Walsh, *Chem. Sci.*, 2015, **6**, 3674–3683.

65 J. L. C. Rowsell, A. R. Millward, K. S. Park and O. M. Yaghi, *J. Am. Chem. Soc.*, 2004, **126**, 5666–5667.

66 J.-W. Yoon, J.-H. Kim, C. Kim, H. W. Jang and J.-H. Lee, *Adv. Energy Mater.*, 2021, **11**, 2003052.

67 Y. Zhang, H. Xiao, X. Zhou, X. Wang and Z. Li, *Ind. Eng. Chem. Res.*, 2017, **56**, 8689–8696.

68 R. Hajjar, C. Volkringer, T. Loiseau, N. Guillou, J. Marrot, G. Férey, I. Margiolaki, G. Fink, C. Morais and F. Taulelle, *Chem. Mater.*, 2011, **23**, 39–47.

69 J. Hedlund, G. Garcia, M. Balsamo, M. Zhou and J. Mouzon, *Sep. Purif. Technol.*, 2021, **277**, 119483.

70 J. Merel, M. Clausse and F. Meunier, *Ind. Eng. Chem. Res.*, 2008, **47**, 209–215.

71 F. Raganati, M. Bellusci, F. Leardi, F. Varsano and P. Ammendola, *Chem. Eng. J.*, 2025, **506**, 159966.

72 F. Fischer, W. Lutz, J.-C. Buhl and E. Laevemann, *Microporous Mesoporous Mater.*, 2018, **262**, 258–268.

7438 | *Energy Environ. Sci.*, 2025, **18**, 7427–7439

This journal is © The Royal Society of Chemistry 2025

73 W. A. Belding, M. P. F. Delmas and W. D. Holeman, *Appl. Therm. Eng.*, 1996, **16**, 447–459.

74 A. Sinha and M. J. Realff, *AIChE J.*, 2019, **65**, e16607.

75 K. N. Son, G. E. Cmarik, J. C. Knox, J. A. Weibel and S. V. Garimella, *J. Chem. Eng. Data*, 2018, **63**, 1663–1674.

76 E. Scuiller, P. Dutournié, M. Zbair and S. Bennici, *J. Chem. Eng. Data*, 2023, **68**, 1865–1871.

77 *U.S. Energy Information Administration, International Energy Outlook 2023*, 2023.

78 *U.S. Energy Information Administration*, https://www.eia.gov/todayinenergy/detail.php?id=60262, (accessed February, 2025).

79 S. Alvik, *Hydrogen forecast to 2050*, DNV AS, 2022.

80 L. Cozzi, T. Gül, S. Bouckaert, A. Fernandez Pales, C. McGlade, U. Remme, B. Wanner, L. Varro, D. D'Ambrosio and T. Spencer, *Net Zero by 2050, A Roadmap for the Global Energy Sector*, International Energy Agency, 2021.

81 A. Gambhir, S. Mittal, R. D. Lamboll, N. Grant, D. Bernie, L. Gohar, A. Hawkes, A. Köberle, J. Rogelj and J. A. Lowe, *Nat. Commun.*, 2023, **14**, 5117.

82 M. Winning, J. Price, P. Ekins, S. Pye, J. Glynn, J. Watson and C. McGlade, *Clim. Policy*, 2019, **19**, 947–958.

83 D. Dubbeldam, S. Calero, D. E. Ellis and R. Q. Snurr, *Mol. Simul.*, 2016, **42**, 81–101.

84 A. K. Rappe, C. J. Casewit, K. S. Colwell, W. A. Goddard, III and W. M. Skiff, *J. Am. Chem. Soc.*, 1992, **114**, 10024–10035.

85 J. J. Potoff and J. I. Siepmann, *AIChE J.*, 2001, **47**, 1676–1682.

86 T. F. Willems, C. H. Rycroft, M. Kazi, J. C. Meza and M. Haranczyk, *Microporous Mesoporous Mater.*, 2012, **149**, 134–141.

87 Y. Higuchi, M. Sugita, S. Moriya, T. Takewaki and S. Tanaka, *Microporous Mesoporous Mater.*, 2024, **374**, 113137.

88 S. Lee, J. H. Lee and J. Kim, *Korean J. Chem. Eng.*, 2018, **35**, 214–221.

This journal is © The Royal Society of Chemistry 2025

Energy Environ. Sci., 2025, **18**, 7427–7439 | 7439